First-principles prediction of ideal type-II Weyl phonons in wurtzite ZnSe

Peng-Fei Liu,[1,2] Jingyu Li,[3] Xin-Hai Tu,[1,2] Hang Li,[4] Junrong Zhang,[1,2] Ping Zhang,[5,6] Qiang Gao,[7,*] and Bao-Tian Wang[1,2,5,8,†]

[1]*Institute of High Energy Physics, Chinese Academy of Sciences (CAS), Beijing 100049, China*
[2]*Spallation Neutron Source Science Center (SNSSC), Dongguan 523803, China*
[3]*Key Laboratory of Materials Physics, Institute of Solid State Physics, HFIPS, Chinese Academy of Sciences, Hefei 230031, China*
[4]*School of Physics and Electronics, Henan University, Kaifeng 475004, China*
[5]*School of Physics and Physical Engineering, Qufu Normal University, Qufu 273165, China*
[6]*Institute of Applied Physics and Computational Mathematics, Beijing 100088, China*
[7]*School of Electronic and Information Engineering, Beihang University, Beijing 100191, China*
[8]*Collaborative Innovation Center of Extreme Optics, Shanxi University, Taiyuan, Shanxi 030006, China*

(Received 2 November 2020; accepted 22 February 2021; published 22 March 2021)

Weyl materials, exhibiting topologically nontrivial touching points in band dispersion, are fascinating subjects of research, which have been extensively studied in electron-related systems. In this paper, by employing first-principles calculations of topological phonons in wurtzite-structured phases of MX chalcogenides (where $M =$ Zn and Cd and $X =$ O, S, Se, and Te), we demonstrate the existence of ideal type-II Weyl phonons in wurtzite ZnSe, a well-known II-VI semiconductor. There are in the $\mathbf{q}_z = 0.0$ plane six pairs of Weyl points stemming from the inversion between the two optical branches. The nontrivial phonon surface states and surface arcs projected on the semifinite (0001) surfaces are investigated. Phonon surface arcs connecting each pair of Weyl points with opposite chirality, guaranteed to be 0.55 Å^{-1} and very long, are readily observable in experiment. The opposite chirality of Weyl points with quantized Berry curvature produces the Weyl phonon Hall effect. Our results propose a potential platform for future experimental study of type-II Weyl phonons in realistic materials.

DOI: 10.1103/PhysRevB.103.094306

I. INTRODUCTION

Topological phases of matter can host analogs of particles relevant for high-energy physics and may enable fresh pathways for the application of quantum materials [1–4]. A more recent example is the experimental discovery of left- and right-handed chiral Weyl fermions as quasiparticles in Weyl semimetal TaAs by addressing the Fermi arcs in angle-resolved photoemission spectra [5,6], which brings the Weyl equation [7] into the experimental realm. Weyl semimetals are crystalline solids hosting emergent Weyl fermions which are the crossing points of two nondegenerate linearly dispersing energy bands in the three-dimensional (3D) momentum space. At the Weyl point (WP), the Fermi surface usually shrinks into a point with a nonzero topological charge ($\mathcal{C} = +1$ or -1) according to the Nielsen-Ninomiya theorem [8]. Each WP acts as a monopole of the Berry curvature field, which leads to topological boundary states on the surface. The topological surface state connects the WPs in pairs with opposite chirality [3,9], forming an unclosed curve in the Fermi surface. According to the geometry of the dispersing energy bands and Fermi surfaces at the WP, Weyl semimetals can be classified into type I and type II [10,11]. In type-I Weyl semimetals, a linear crossing of two bands occurs at the Fermi level with the standard conical energy dispersion, collapsing into a pointlike Fermi surface [12]. As for type-II Weyl semimetals, tilted Weyl cones appear with Fermi surfaces consisting of touched electron-hole pockets [11], which could break the topological Lorentz invariance at the energy of the WP and lead to many unusual electromagnetic responses [13–17]. To date, two broad categories, relying on breaking either time-reversal symmetry $\mathcal{T}$ or spatial symmetry $\mathcal{P}$ (or possibly both), have boosted discovery of Weyl semimetals of electronic fermions in both experiment and theory [18].

As the counterpart of electrons, phonons are the population of quasiparticles describing the collective motion of the underlying atoms [19] and are crucial to many physical properties and the behavior of crystalline materials, such as thermal conductivity [20,21], mechanical properties [22], phase transition [23], superconductivity [24–26], and other properties related to vibrational modes [27]. Similar to topologically nontrivial fermions of electrons, there are also unconventional topological vibrational phonons which have been experimentally observed in the 3D momentum space of solid crystals by using inelastic x-ray scattering experiments, such as double Weyl phonons in parity-breaking FeSi [28,29] and phononic helical nodal lines with $\mathcal{PT}$ protection in MoB_2 [30]. In the meantime, intensive efforts have been devoted to exploring topological phonons in materials via first-principles methods, and thus a number of candidates have been predicted to host nontrivial states [31], such as Dirac phonons (two-dimensional materials of CrI_3, YGaI, CuI, and group V

*gaoqiang@buaa.edu.cn
†wangbt@ihep.ac.cn

elements) [32], WPs {In_2Te_3 [33], wurtzite cuprous iodide (CuI) [34], zinc-blende CdTe [35], LiCaAs [31], cubic $SrSi_2$ [36], $K_2Sn_2O_3$ [37], WC-type materials [38], and BaPtGe [39]}, nodal-line topological phonons (ZrSiO [33], MgB_2 [40], ScZn [31], and $Rb_2Sn_2O_3$ [41]), nodal-ring phonons (graphene [42], $CaMg_2$ [43], and bcc C_8 [44]), topological triple-point phonons (silicon [45]), and triangular Weyl phonons (YPt_2B and α-SiO_2) [46], which greatly enrich the family of topological phonon materials.

As opposed to electronic fermions, phonons, being the most basic emergent boson of crystalline lattices and not limited by the Pauli exclusion principle [19], could be physically probed within the scale of terahertz frequency in a phonon spectrum [47]. In general, nondegenerate two-phonon bands touching in the Brillouin zone (BZ) could give rise to the possible appearance of WPs in 3D materials due to the absence of spin degrees of freedom for phonons [34,35]. This feature of phonons provides an ideal platform for studying topological Weyl bosonic excitations in realistic materials. Ideal Weyl phonons should have a relatively large separation with the same energy in the 3D momentum space and be separated from any other phonon bands [34,48]. These features are in favor of the observation of topological nontrivial surface states in experiments and the further development of Weyl physics. Amongst all the predicted realistic candidates [29–31,34,35,38,46,49], rare phonons have been found to satisfy the above criteria for ideal type-II WPs. In this case, exploring the ideal type-II Weyl phonons with clean surface states is still a priority to guide efforts in experiment and theory.

In this paper, based on first-principles calculations, we make a screening of topological type-II Weyl phonons in wurtzite-structured phases of MX chalcogenides (where $M =$ Zn and Cd and $X =$ O, S, Se, and Te). We demonstrate that wurtzite ZnSe hosts the ideal type-II Weyl phonons with six pairs of accidentally degenerated WPs at the frequency of 5.49 THz in the $\mathbf{q}_z = 0.0$ plane. The WPs originate from a band inversion between the two optical branches. We observe that clear phonon Fermi arcs connect two WPs of opposite chirality and vanish in the bulk phonon continuum in the surface state calculations. Each pair of WPs with quantized opposite Berry curvature are well separated by a distance of 0.55 $Å^{-1}$ in the momentum space, suggesting that wurtzite ZnSe is a promising material candidate for studying the type-II Weyl phonons and phonon Fermi-arc surface states experimentally.

II. COMPUTATIONAL METHODS

First-principles calculations were performed at the density functional theory level using the Vienna *ab initio* simulation package [50]. The Perdew-Burke-Ernzerhof generalized gradient approximation revised for solids [51,52] was selected to describe the exchange-correlation energy. The projector augmented-wave method [53,54] was used to treat the interactions between ions and valence electrons with a plane-wave cutoff energy of 500 eV. The full BZ was sampled with a $15 \times 15 \times 7$ Monkhorst-Pack **k** mesh [55]. All geometric structures were fully relaxed until the residual forces on each atom were less than 0.01 eV/Å. The real-space interatomic force constants were calculated with a $4 \times 4 \times 2$ supercell

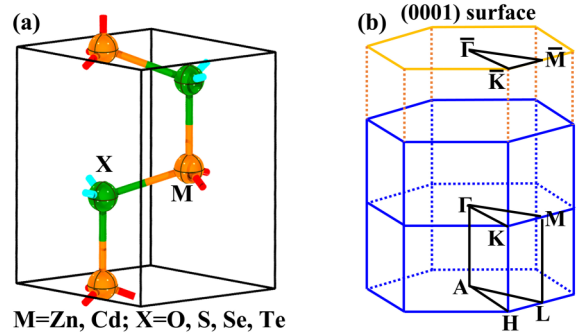

FIG. 1. (a) Crystal structure of wurtzite MX (where $M =$ Zn and Cd and $X =$ O, S, Se, and Te) chalcogenides. Orange and green spheres denote the M and X atoms, respectively. (b) BZ and the projected surface BZ for the (0001) surface of wurtzite MX chalcogenides.

by the finite-displacement method [56] using the PHONOPY package [57] with the following equation:

$$\Phi_{\alpha\beta}(\mathbf{R}_{jl} - \mathbf{R}_{j'l'}) = \frac{\partial^2 V}{\partial u^{\alpha}_{jl} \partial u^{\beta}_{j'l'}} = -\frac{\partial F_{\beta}(\mathbf{R}_{j'l'})}{\partial u^{\alpha}_{jl}} \simeq -\frac{F_{\beta}\left(\mathbf{R}_{j'l'}; \Delta u^{\alpha}_{jl}\right) - F_{\beta}(\mathbf{R}_{j'l'})}{\Delta u^{\alpha}_{jl}}, \quad (1)$$

where V represents the potential energy, $\{\alpha, \beta\} = (x, y, z)$ are the Cartesian indices, $F_{\beta}(\mathbf{R}_{j'l'})$ is the force of the l'th atom in the j'th unit cell along the β direction, and u^{α}_{jl} ($u^{\beta}_{j'l'}$) is the displacement component of the lth (l'th) atom in the jth (j'th) unit cell along the α (β) direction. Since wurtzite-structured phases of MX chalcogenides are polar materials, the nonanalytical term correction has been considered in the dynamical matrix to avoid the degeneracy of optical branches when $\mathbf{q}$ goes to zero [58,59]. We also used some already existent force constant data from a public phonon database [60,61]. The Wannier tight-binding Hamiltonian of phonons was constructed from real-space interatomic force constants [43,62] which can be described by

$$H = \frac{1}{2} \sum_{l,m,\alpha} \sum_{l',m',\beta} \Phi_{\alpha\beta}(\mathbf{R}_{jl} - \mathbf{R}_{j'l'}) u^{\alpha}_{lm} u^{\beta}_{l'm'}. \quad (2)$$

The nontrivial boundary-edged phonon states were calculated from the imaginary part of the surface Green's function [63] as provided by the open-source software WANNIERTOOLS [64].

III. RESULTS AND ANALYSIS

A. Crystal structure

As an important kind of semiconductor, MX chalcogenides (where $M =$ Zn and Cd and $X =$ O, S, Se, and Te) in general have two types of crystal phase, cubic blende and hexagonal wurtzite, which could be selectively synthesized via different chemical methods [65,66]. Wurtzite MX chalcogenides, illustrated in Fig. 1(a), crystallize in a noncentrosymmetric hexagonal space group of $P6_3mc$ (No. 186) with 2 f.u. and four atoms per unit cell. The structure can be considered as being formed by the penetration of two hexagonal closest packing lattices in the same 6_3 axis [67], with one of them

TABLE I. The calculated lattice constants (l_a and l_c in angstroms), bond lengths of M-X ($l_{M\text{-}X}$ in angstroms), and parameters d for MX chalcogenides.

Compound	l_a	l_c	$l_{M\text{-}X}$	d ($\times 10^{-2}$)
ZnO	3.238	5.227	1.980/1.973	6.05
ZnS	3.782	6.207	2.322/2.319	6.29
ZnSe	3.977	6.533	2.443/2.439	6.30
ZnTe	4.281	7.035	2.629/2.627	6.31
CdO	3.684	5.825	2.246/2.229	5.72
CdS	4.123	6.710	2.526/2.521	6.18
CdSe	4.303	7.015	2.636/2.633	6.21
CdTe	4.580	7.502	2.809/2.807	6.28

being displaced with respect to the other. In the wurtzite structure, there are two crystallographically distinct Wyckoff positions for M atoms and X atoms. The positions of the atoms are given by M 2b $(\frac{1}{3}, \frac{2}{3}, \frac{1}{2} - d)$ and X 2b $(\frac{2}{3}, \frac{1}{3}, \frac{1}{2} + d)$, respectively, with a parameter d for wurtzite MX chalcogenides. Each atom is featured with tetrahedral symmetry; that is, an atom is fourfold coordinated to four other atoms of the same kind. In terms of cell symmetry, the length of the vertical M-X bonds is slightly larger than that of the diagonally oriented M-X bonds, giving rise to the distorted tetrahedral structure in wurtzite MX chalcogenides. More details about the lattice parameters of wurtzite MX chalcogenides are listed in Table I. Our calculated results are in good agreement with experimental results [65,66,68] and other calculated values [58,69]. The bulk hexagonal BZ and the corresponding (0001) surface BZ are given in Fig. 1(b).

B. Phonon Weyl points

The phonon dispersions of wurtzite MX chalcogenides are shown in Fig. 2(a) and Supplemental Material Figs. S1–S8

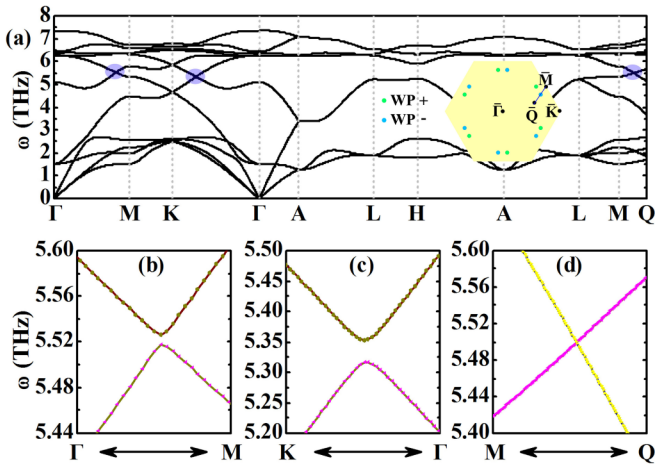

FIG. 2. (a) Calculated phonon dispersion of wurtzite ZnSe along the high-symmetry momentum path. The phonon WP along the blue line indicated in the inset is shown in the right section of the phonon dispersion along the M-Q line with the shadow color. (b)–(d) The enlarged phonon dispersions of the blue shadow regions shown in Fig. 2(a). The colorful lines in the phonon dispersions highlight different vibrational modes.

[70]. For ZnO, ZnS, ZnSe, ZnTe, CdS, CdSe, and CdTe, the absence of unstable vibrational modes in the BZ indicates the dynamical stability of these crystals. In contrast, wurtzite CdO is unstable, with the result of an imaginary frequency around the Γ point, stemming predominantly from vibrations of Cd and O atoms along the $\mathbf{q}_z$ direction. Since the primitive cell contains four atoms with two M and two X atoms in the wurtzite structure, there are 12 phonon branches for any chosen $\mathbf{q}$ point in total dispersions: 3 acoustic and 9 optical modes. When going from $X = $ O, to S, to Se, to Te with increasing mass, the optical phonon branches of the wurtzite MX chalcogenides shift to a lower-frequency region and get close to each other. This makes optical branches touch at some points. At first glance, there is a tiny gap along the Γ-M and Γ-K directions between the third and fourth optical branches (the sixth and seventh phonon branches) in the phonon dispersions of wurtzite ZnSe and CdTe. This indicates the possibility of WPs existing in it. After carefully checking the phonon dispersions with a much denser grid of momentum points in BZ, we find that the wurtzite CdTe has a full energy gap between the third and fourth optical branches throughout the whole BZ without Weyl phonons. In wurtzite ZnSe, the frequency gaps finally approach zero and form Weyl points at 12 positions (shown in Table S1 [70]) in the $\mathbf{q}_z = 0.0$ plane around the optical phonon frequency of 5.40 THz in Fig. 2(d). This is similar to wurtzite CuI [34], which also has ideal type-II phonon Weyl points.

To clarify the origin of the Weyl points, the phonon branches have been sorted with different colors according to the continuity of the eigenvectors by the phononic $\mathbf{k} \cdot \mathbf{p}$ theorem [71,72] as follows:

$$\left| \sum e^*_{k,\sigma_1}(j) \cdot e_{k+\triangle,\sigma_2}(j) \right| = \left| \delta_{\sigma_1,\sigma_2} - o(\triangle) \right|, \qquad (3)$$

where $e^*_{k,\sigma}(j)$ is the displacement of the atom j in the eigenvector of the (k, σ) vibrational mode and $\triangle$ is a small wave vector. Far away from the Weyl point in Figs. 2(b) and 2(c), the red state is the sixth phonon branch and energetically lower than the yellow state (the seventh phonon branch). When getting close to the Weyl point in Fig. 2(d), the two bands have inverted energy order with the phonon band inversion in analogy to the topological electronic structure [73,74]. Atomic vibrations of both Zn and Se atoms contribute to those two optical branches. The vibrations of the touching points are derived from the rotations of the Zn and Se atoms, while the positions of all atoms remain unchanged.

Since the structure of wurtzite ZnSe belongs to the point group C_{6v}, its reciprocal space holds the mirror symmetries σ_v $(-\mathrm{q}_x, \mathrm{q}_y)$, sixfold rotational symmetry $C_{6z} = (\frac{q_x}{2} - \frac{\sqrt{3}q_y}{2}, \frac{\sqrt{3}q_x}{2} + \frac{q_y}{2}, q_z)$, and time-reversal symmetry $\mathcal{T}$. On the basis of these symmetries, 12 WPs are periodically distributed in the momentum space with accidental degeneracy and could not locate at in-plane high-symmetry lines, as shown schematically in the inset of Fig. 2, which is the same as wurtzite CuI [34]. A perspective 3D plot of the corresponding one pair of WPs is presented in Fig. 3(a). It is clear that the two bands touch with linear dispersions. In order to identify the type of these WPs, an enlarged 2D view of one point is displayed in Fig. 3(b). Both linear crossing bands show tilted contacts with

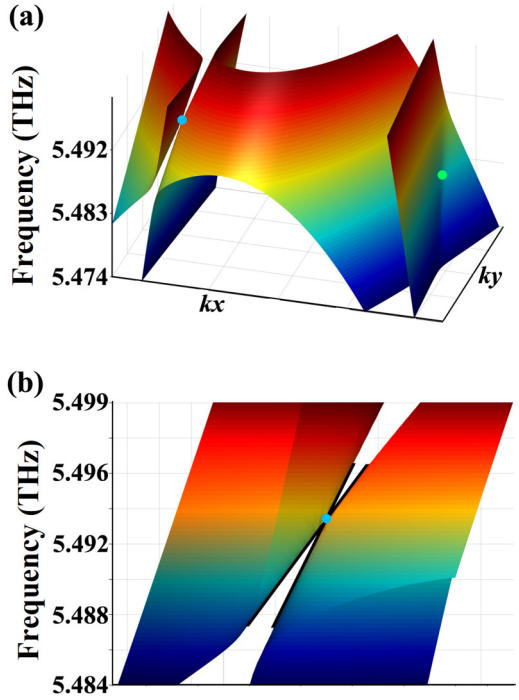

FIG. 3. (a) Perspective plot of the phonon WPs with positive and negative charge in the 3D momentum space. (b) The zoomed-in crossing phonon dispersion around one phonon WP. The WPs with opposite chirality are marked with different colors.

homochromous velocity along one direction, indicating that the 12 WPs are typical type II. It should be noticed that the gap out of the $\mathbf{q}_z = 0.0$ plane between the third and fourth optical branches is relatively large, as shown in Fig. 2. This feature can give rise to the benefit of experimental observations of exotic topological bosons. So, wurtzite ZnSe is an ideal material harboring type-II Weyl phononic points.

C. Topological charges and surface states

To confirm the topological properties of these gapless points, we calculate the Berry curvature [64] via

$$\Omega_n^z(\mathbf{q}) = \nabla_{\mathbf{q}} \times i\langle u_n(\mathbf{q})|\nabla_{\mathbf{q}}|u_n(\mathbf{q})\rangle, \tag{4}$$

where $u_n(\mathbf{q})$ represents the phonon eigenmodes of the nth phonon band. Usually, one pair of Weyl nodes could show the positive and negative Berry curvature distributions, which can be regarded as the source and sink of Berry curvature in the momentum space, respectively. As drawn in Figs. 4(a) and 4(b), it clearly shows the monopolelike distribution of the Berry curvature around two crossing nodes in the $\mathbf{q}_z = 0.0$ plane. As a long-pursued topic in topological materials, WPs host well-defined chiral charges with opposite signs [75], whose chirality is calculated by integrating the Berry curvature on a closed surface in the 3D BZ enclosing the corresponding WP as follows [76,77]:

$$\gamma_n = \oint_C \Omega_n(\mathbf{q}) \cdot d\mathbf{q}. \tag{5}$$

Figures 4(c) and 4(d) present the Wannier center evolutions around the two points with opposite charges ± 1, which

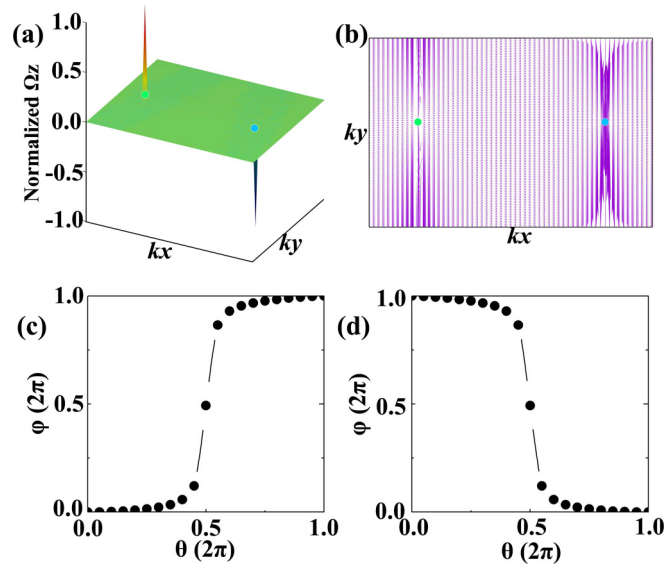

FIG. 4. (a) and (b) Normalized Berry curvature Ω_z of wurtzite ZnSe surrounding a pair of the phonon WPs with positive and negative charge on the $\mathbf{q}_z = 0.0$ plane of the BZ. The length of each arrow is the magnitude of the in-plane Berry curvature. (c) and (d) The Wannier center evolution around WPs with (c) positive and (d) negative charges, respectively. Here, θ is the polar angle of orbitals, and φ shows the phase factor of the position operator on the orbitals.

correspond to the source and sink of the Berry curvature distributions, respectively. Furthermore, we determine the topological charges of all the WPs of wurtzite ZnSe in the inset of Fig. 2 and in Table S1 [70], which shows a distribution similar to that of wurtzite CuI [34], giving six WPs with $\mathcal{C} = +1$ and six WPs with $\mathcal{C} = -1$ in pairs.

To clearly verify the type-II WPs, we calculate the topologically protected nontrivial surface states and Fermi arcs of

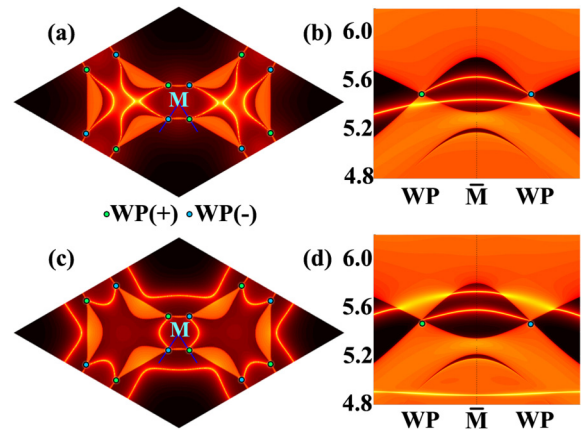

FIG. 5. (a) The surface arcs for wurtzite ZnSe projected onto the top (0001) surface (Zn-terminated surface) at the frequency of 5.49 THz. It is observed that the surface arc always connects two WPs with the opposite charges. (b) Surface band structure along the blue lines indicated in (a). (c) and (d) Same as (a) and (b), respectively, but for the bottom $(000\bar{1})$ surface (Se-terminated surface). The length of one pair of WPs connecting with the topological surface arcs is near 0.55 Å^{-1}.

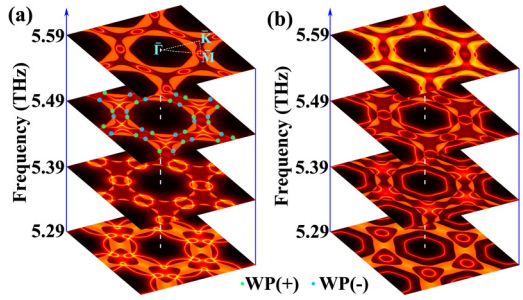

FIG. 6. The frequency-dependent evolution of the topologically protected phononic nontrivial surface states of wurtzite ZnSe for (a) Zn-terminated and (b) Se-terminated (0001) surfaces.

phonons in the momentum space containing the phonon WPs with opposite chirality. The different-colored spheres in Fig. 5 denote the phonon WPs with oppositely charged chirality of $\mathcal{C} = +1$ or -1, respectively. On the Zn-terminated surface in Fig. 5(a), there are interesting topological surface arcs which typically connect each pair of phonon WPs with opposite chirality at the exact frequency of 5.494 THz. One can clearly see the arc-shaped dispersing states around the phonon WPs, contributing to the the candidate topological arcs. Figure 5(b) depicts the surface phonon dispersion along the blue lines indicated in Fig. 5(a). It can be seen that the topologically protected surface states of Weyl phonons with isotropy actually exist within the phonon bulk bands of wurtzite ZnSe. In Fig. 5(b), there are also additional trivial surface states crossing bulk pocket bands below the phonon WPs. As for the Se-terminated surface, the phonon bulk states harbor very clean surface arcs forming M-centered closed circles with trivial surface states coming into being as Γ-centered closed hexagons in Fig. 5(c). The distance of a pair of WPs connecting with topological phonon surface arcs is about 0.55 Å^{-1} (30% of the reciprocal lattice constants), which is much larger than Weyl phonon material (wurtzite cuprous iodide CuI) [34] and Weyl fermion semimetal TaAs [5,6]. In Fig. 5(d), the corresponding nontrivial surface states and irrelevant trivial states crossing bulk bands above phonon WPs are observed in the surface phonon dispersion, agreeing with the foregoing 2D surface arcs projected onto the (0001) surface. In addition, one trivial surface state below the phonon WPs exists in phonon bulk bands in Fig. 5(d). These boundary-dependent surface states reasonably correspond to the bulk topological charges and Berry curvatures, confirming that the wurtzite ZnSe indeed hosts nontrivially topological Weyl phonons. In addition, we also calculate the frequency-dependent evolutions of the arc states connecting the type-II WPs with the surface spectral function being fixed at phonon frequencies of 5.29, 5.39, 5.49, and 5.59 THz on the ZnSe(0001) (Zn-terminated) surface and the ZnSe($000\bar{1}$) (Se-terminated) surface in Fig. 6. Certainly, there are interesting topological surface arcs which typically connect each pair of phonon WPs. These results are in good agreement with the numerical predictions shown in Fig. 5.

It has been established that accidental degeneracy, which occurs coincidentally without any protection by symmetry in a 3D reciprocal space, could give rise to the possible existence of Weyl points in both electron [78] and phonon structures [34]. For wurtzite ZnSe, the 12 Weyl points are also induced by accidental degeneracy, which is similar to that of wurtzite CuI. For a given point in the phonon spectrum of wurtzite ZnSe, it will certainly exist at or off high-symmetry momentum lines. Previous results have demonstrated that WPs cannot locate at any high-symmetry momentum lines with the point group C_{6v} in wurtzite CuI [34]. Thus the WPs surely locate off high-symmetry lines and stem from time-reversal symmetry $\mathcal{T}$. Besides the above-mentioned ideal Weyl points, we also find another 24 Weyl points at the phonon frequency of ∼6.48 THz (shown in Table S1 and Fig. S9 [70]). With the operations of σ_v and C_{6z}, the 24 Weyl points locate in two planes of $\mathbf{q}_z = \pm 0.3523$ with a similar distribution to that described above. What is more, we predict that wurtzite ZnSe hosts the well-defined phononic topological Weyl nodal lines [40] in its bulk phonon spectrum. We have shown them in Fig. S10 [70]. It is clearly observable that countless WPs, which are always paired in the opposite Berry phase, extend the whole surface Brillouin zone through the high-symmetry boundary with countless broken surface arc states in Fig. S11 [70]. This feature is also predicted in the Weyl phonon lines of MgB_2 [40].

IV. CONCLUSIONS

In summary, on the basis of first-principles calculations, we find that wurtzite ZnSe hosts ideal type-II Weyl phonons in the $\mathbf{q}_z = 0.0$ plane at the equilibrium volume. The six pairs of WPs have minimal hybridization between the Weyl nodes and the bulk bands, which is guaranteed to be readily detectable in experiments. The Fermi-arc surface states connecting the WPs with opposite chirality are very clean and could be easily distinguished by the Zn- and Se-terminated surfaces. Each pair of the degenerated WPs with the splitting distance of about 0.55 Å^{-1} shows the opposite quantized Berry curvature, which could produce the Weyl phonon Hall effect [79,80]. Besides, we also find 24 Weyl points that locate in two planes of $\mathbf{q}_z = \pm 0.3523$ at the phonon frequency of ∼6.48 THz and so-called phononic topological Weyl nodal lines [40] in the phonon spectrum of wurtzite ZnSe. Our work points out a real material for studying ideal type-II phononic topological WPs and is useful to advance the fabrication of topological phonon devices.

ACKNOWLEDGMENTS

The authors gratefully acknowledge financial support from the Ph.D. Start-up Fund of the Natural Science Foundation of Guangdong Province of China (Grant No. 2018A0303100013), Science Challenge Project (Grant No. TZ2016001), and Natural Science Foundation of China (Grants No. 11804078, No. 11675195, No. 11805214, and No. 12074381). The authors also are thankful for the computational resources from the Supercomputer Centre of the China Spallation Neutron Source.

[1] C.-K. Chiu, J. C. Y. Teo, A. P. Schnyder, and S. Ryu, Classification of topological quantum matter with symmetries, Rev. Mod. Phys. **88**, 035005 (2016).

[2] Y. Ando and L. Fu, Topological crystalline insulators and topological superconductors: From concepts to materials, Annu. Rev. Condens. Matter Phys. **6**, 361 (2015).

[3] B. Yan and C. Felser, Topological materials: Weyl semimetals, Annu. Rev. Condens. Matter Phys. **8**, 337 (2017).

[4] B. Yan and S.-C. Zhang, Topological materials, Rep. Prog. Phys. **75**, 096501 (2012).

[5] S.-Y. Xu, I. Belopolski, N. Alidoust, M. Neupane, G. Bian, C. Zhang, R. Sankar, G. Chang, Z. Yuan, C.-C. Lee, S.-M. Huang, H. Zheng, J. Ma, D. S. Sanchez, B. Wang, A. Bansil, F. Chou, P. P. Shibayev, H. Lin, S. Jia *et al.*, Discovery of a Weyl fermion semimetal and topological Fermi arcs, Science **349**, 613 (2015).

[6] B. Q. Lv, H. M. Weng, B. B. Fu, X. P. Wang, H. Miao, J. Ma, P. Richard, X. C. Huang, L. X. Zhao, G. F. Chen, Z. Fang, X. Dai, T. Qian, and H. Ding, Experimental Discovery of Weyl Semimetal TaAs, Phys. Rev. X **5**, 031013 (2015).

[7] P. B. Pal, Dirac, Majorana, and Weyl fermions, Am. J. Phys. **79**, 485 (2011).

[8] H. B. Nielsen and M. Ninomiya, Absence of neutrinos on a lattice, Nucl. Phys. B **185**, 20 (1981).

[9] M. Z. Hasan, S.-Y. Xu, I. Belopolski, and S.-M. Huang, Discovery of Weyl fermion semimetals and topological Fermi arc states, Annu. Rev. Condens. Matter Phys. **8**, 289 (2017).

[10] S. Tchoumakov, M. Civelli, and M. O. Goerbig, Magnetic-Field-Induced Relativistic Properties in Type-I and Type-II Weyl Semimetals, Phys. Rev. Lett. **117**, 086402 (2016).

[11] A. A. Soluyanov, D. Gresch, Z. Wang, Q. Wu, M. Troyer, X. Dai, and B. A. Bernevig, Type-II Weyl semimetals, Nature (London) **527**, 495 (2015).

[12] H. Weng, C. Fang, Z. Fang, B. A. Bernevig, and X. Dai, Weyl Semimetal Phase in Noncentrosymmetric Transition-Metal Monophosphides, Phys. Rev. X **5**, 011029 (2015).

[13] A. Tamai, Q. S. Wu, I. Cucchi, F. Y. Bruno, S. Riccò, T. K. Kim, M. Hoesch, C. Barreteau, E. Giannini, C. Besnard, A. A. Soluyanov, and F. Baumberger, Fermi Arcs and Their Topological Character in the Candidate Type-II Weyl Semimetal $MoTe_2$, Phys. Rev. X **6**, 031021 (2016).

[14] L. Huang, T. M. McCormick, M. Ochi, Z. Zhao, M.-T. Suzuki, R. Arita, Y. Wu, D. Mou, H. Cao, J. Yan, N. Trivedi, and A. Kaminski, Spectroscopic evidence for a type II Weyl semimetallic state in $MoTe_2$, Nat. Mater. **15**, 1155 (2016).

[15] T.-R. Chang, S.-Y. Xu, D. S. Sanchez, W.-F. Tsai, S.-M. Huang, G. Chang, C.-H. Hsu, G. Bian, I. Belopolski, Z.-M. Yu, S. A. Yang, T. Neupert, H.-T. Jeng, H. Lin, and M. Z. Hasan, Type-II Symmetry-Protected Topological Dirac Semimetals, Phys. Rev. Lett. **119**, 026404 (2017).

[16] Z.-M. Yu, Y. Yao, and S. A. Yang, Predicted Unusual Magnetoresponse in Type-II Weyl Semimetals, Phys. Rev. Lett. **117**, 077202 (2016).

[17] M. Udagawa and E. J. Bergholtz, Field-Selective Anomaly and Chiral Mode Reversal in Type-II Weyl Materials, Phys. Rev. Lett. **117**, 086401 (2016).

[18] H. Gao, J. W. F. Venderbos, Y. Kim, and A. M. Rappe, Topological semimetals from first principles, Annu. Rev. Mater. Research **49**, 153 (2019).

[19] H. R. Schober, Introduction to lattice dynamics, in *Interstitial Intermetallic Alloys* (Springer, Dordrecht, 1995), pp. 197–223.

[20] G. L. Guthrie, Longitudinal and transverse phonons in lattice thermal conductivity, Phys. Rev. B **3**, 3573 (1971).

[21] X. Li, P.-F. Liu, E. Zhao, Z. Zhang, T. Guidi, M. D. Le, M. Avdeev, K. Ikeda, T. Otomo, M. Kofu, K. Nakajima, J. Chen, L. He, Y. Ren, X.-L. Wang, B.-T. Wang, Z. Ren, H. Zhao, and F. Wang, Ultralow thermal conductivity from transverse acoustic phonon suppression in distorted crystalline α-MgAgSb, Nat. Commun. **11**, 942 (2020).

[22] Z. Tang and N. R. Aluru, Calculation of thermodynamic and mechanical properties of silicon nanostructures using the local phonon density of states, Phys. Rev. B **74**, 235441 (2006).

[23] P. A. Fleury, J. F. Scott, and J. M. Worlock, Soft Phonon Modes and the 110° K Phase Transition in $SrTiO_3$, Phys. Rev. Lett. **21**, 16 (1968).

[24] K.-P. Bohnen, R. Heid, and B. Renker, Phonon Dispersion and Electron-Phonon Coupling in MgB_2 and AlB_2, Phys. Rev. Lett. **86**, 5771 (2001).

[25] P.-F. Liu and B.-T. Wang, Face-centered cubic MoS_2: A novel superconducting three-dimensional crystal more stable than layered T-MoS_2, J. Mater. Chem. C **6**, 6046 (2018).

[26] C.-B. Zhang, W.-D. Li, P. Zhang, and B.-T. Wang, Phase transition, elasticity, phonon spectra, and superconductive properties of equiatomic TiZr, TiHf, and ZrHf alloys at high pressure: *Ab initio* calculations, Comput. Mater. Sci. **178**, 109637 (2020).

[27] A. Togo and I. Tanaka, First principles phonon calculations in materials science, Scr. Mater. **108**, 1 (2015).

[28] H. Miao, T. T. Zhang, L. Wang, D. Meyers, A. H. Said, Y. L. Wang, Y. G. Shi, H. M. Weng, Z. Fang, and M. P. M. Dean, Observation of Double Weyl Phonons in Parity-Breaking FeSi, Phys. Rev. Lett. **121**, 035302 (2018).

[29] T. Zhang, Z. Song, A. Alexandradinata, H. Weng, C. Fang, L. Lu, and Z. Fang, Double-Weyl Phonons in Transition-Metal Monosilicides, Phys. Rev. Lett. **120**, 016401 (2018).

[30] T. T. Zhang, H. Miao, Q. Wang, J. Q. Lin, Y. Cao, G. Fabbris, A. H. Said, X. Liu, H. C. Lei, Z. Fang, H. M. Weng, and M. P. M. Dean, Phononic Helical Nodal Lines with $\mathcal{PT}$ Protection in MoB_2, Phys. Rev. Lett. **123**, 245302 (2019).

[31] J. Li, J. Liu, S. A. Baronett, M. Liu, L. Wang, R. Li, Y. Chen, D. Li, Q. Zhu, and X.-Q. Chen, Computation and data driven discovery of topological phononic materials, Nat. Commun. **12**, 1204 (2021).

[32] Y. Jin, R. Wang, and H. Xu, Recipe for Dirac phonon states with a quantized valley Berry phase in two-dimensional hexagonal lattices, Nano Lett. **18**, 7755 (2018).

[33] T. Zhang, L. Lu, S. Murakami, Z. Fang, H. Weng, and C. Fang, Diagnosis scheme for topological degeneracies crossing high-symmetry lines, Phys. Rev. Research **2**, 022066(R) (2020).

[34] J. Liu, W. Hou, E. Wang, S. Zhang, J.-T. Sun, and S. Meng, Ideal type-II Weyl phonons in wurtzite CuI, Phys. Rev. B **100**, 081204(R) (2019).

[35] B. W. Xia, R. Wang, Z. J. Chen, Y. J. Zhao, and H. Xu, Symmetry-Protected Ideal Type-II Weyl Phonons in CdTe, Phys. Rev. Lett. **123**, 065501 (2019).

[36] Z. Huang, Z. Chen, B. Zheng, and H. Xu, Three-terminal Weyl complex with double surface arcs in a cubic lattice, npj Comput. Mater. **6**, 87 (2020).

[37] Q.-B. Liu, Y. Qian, H.-H. Fu, and Z. Wang, Symmetry-enforced Weyl phonons, npj Comput. Mater. **6**, 95 (2020).

[38] J. Li, Q. Xie, S. Ullah, R. Li, H. Ma, D. Li, Y. Li, and X.-Q. Chen, Coexistent three-component and two-component Weyl

phonons in TiS, ZrSe, and HfTe, Phys. Rev. B **97**, 054305 (2018).

[39] T. Zhang, R. Takahashi, C. Fang, and S. Murakami, Twofold quadruple Weyl nodes in chiral cubic crystals, Phys. Rev. B **102**, 125148 (2020).

[40] J. Li, Q. Xie, J. Liu, R. Li, M. Liu, L. Wang, D. Li, Y. Li, and X.-Q. Chen, Phononic Weyl nodal straight lines in MgB_2, Phys. Rev. B **101**, 024301 (2020).

[41] Q.-B. Liu, H.-H. Fu, G. Xu, R. Yu, and R. Wu, Categories of phononic topological Weyl open nodal lines and a potential material candidate: $Rb_2Sn_2O_3$, J. Phys. Chem. Lett. **10**, 4045 (2019).

[42] J. Li, L. Wang, J. Liu, R. Li, Z. Zhang, and X.-Q. Chen, Topological phonons in graphene, Phys. Rev. B **101**, 081403(R) (2020).

[43] B. Zheng, B. Xia, R. Wang, Z. Chen, J. Zhao, Y. Zhao, and H. Xu, Ideal type-III nodal-ring phonons, Phys. Rev. B **101**, 100303(R) (2020).

[44] Y. J. Jin, Z. J. Chen, B. W. Xia, Y. J. Zhao, R. Wang, and H. Xu, Ideal intersecting nodal-ring phonons in bcc C_8, Phys. Rev. B **98**, 220103(R) (2018).

[45] Y. Liu, N. Zou, L. Zhao, X. Chen, Y. Xu, and W. Duan, Ubiquitous topological states of phonons in solids: Silicon as a model material, arXiv:2010.00224.

[46] R. Wang, B. W. Xia, Z. J. Chen, B. B. Zheng, Y. J. Zhao, and H. Xu, Symmetry-Protected Topological Triangular Weyl Complex, Phys. Rev. Lett. **124**, 105303 (2020).

[47] N. Choudhury and S. L. Chaplot, Inelastic neutron scattering and lattice dynamics: Perspectives and challenges in mineral physics, in *Neutron Applications in Earth, Energy and Environmental Sciences* (Springer, New York, 2009), pp. 145–188.

[48] B. Yang, Q. Guo, B. Tremain, R. Liu, L. E. Barr, Q. Yan, W. Gao, H. Liu, Y. Xiang, J. Chen, C. Fang, A. Hibbins, L. Lu, and S. Zhang, Ideal Weyl points and helicoid surface states in artificial photonic crystal structures, Science **359**, 1013 (2018).

[49] B. Peng, Y. Hu, S. Murakami, T. Zhang, and B. Monserrat, Topological phonons in oxide perovskites controlled by light, Sci. Adv. **6**, eabd1618 (2020).

[50] G. Kresse and J. Furthmüller, Efficient iterative schemes for *ab initio* total-energy calculations using a plane-wave basis set, Phys. Rev. B **54**, 11169 (1996).

[51] J. P. Perdew, A. Ruzsinszky, G. I. Csonka, O. A. Vydrov, G. E. Scuseria, L. A. Constantin, X. Zhou, and K. Burke, Restoring the Density-Gradient Expansion for Exchange in Solids and Surfaces, Phys. Rev. Lett. **100**, 136406 (2008).

[52] G. I. Csonka, J. P. Perdew, A. Ruzsinszky, P. H. T. Philipsen, S. Lebègue, J. Paier, O. A. Vydrov, and J. G. Ángyán, Assessing the performance of recent density functionals for bulk solids, Phys. Rev. B **79**, 155107 (2009).

[53] G. Kresse and D. Joubert, From ultrasoft pseudopotentials to the projector augmented-wave method, Phys. Rev. B **59**, 1758 (1999).

[54] D. M. Ceperley and B. J. Alder, Ground State of the Electron Gas by a Stochastic Method, Phys. Rev. Lett. **45**, 566 (1980).

[55] H. J. Monkhorst and J. D. Pack, Special points for Brillouin-zone integrations, Phys. Rev. B **13**, 5188 (1976).

[56] S. Baroni, S. De Gironcoli, A. Dal Corso, and P. Giannozzi, Phonons and related crystal properties from density-functional perturbation theory, Rev. Mod. Phys. **73**, 515 (2001).

[57] A. Togo, F. Oba, and I. Tanaka, First-principles calculations of the ferroelastic transition between rutile-type and $CaCl_2$-type SiO_2 at high pressures, Phys. Rev. B **78**, 134106 (2008).

[58] A. Togo, L. Chaput, and I. Tanaka, Distributions of phonon lifetimes in Brillouin zones, Phys. Rev. B **91**, 094306 (2015).

[59] Y. Wang, J. J. Wang, W. Y. Wang, Z. G. Mei, S. L. Shang, L. Q. Chen, and Z. K. Liu, A mixed-space approach to first-principles calculations of phonon frequencies for polar materials, J. Phys.: Condens. Matter **22**, 202201 (2010).

[60] A. Jain, S. P. Ong, G. Hautier, W. Chen, W. D. Richards, S. Dacek, S. Cholia, D. Gunter, D. Skinner, G. Ceder, and K. A. Persson, Commentary: The materials project: A materials genome approach to accelerating materials innovation, APL Mater. **1**, 011002 (2013).

[61] G. Petretto, S. Dwaraknath, H. P. C. Miranda, D. Winston, M. Giantomassi, M. J. van Setten, X. Gonze, K. A. Persson, G. Hautier, and G.-M. Rignanese, High-throughput density-functional perturbation theory phonons for inorganic materials, Sci. Data **5**, 180065 (2018).

[62] Y. Liu, Y. Xu, S.-C. Zhang, and W. Duan, Model for topological phononics and phonon diode, Phys. Rev. B **96**, 064106 (2017).

[63] M. P. Lopez Sancho, J. M. Lopez Sancho, J. M. L. Sancho, and J. Rubio, Highly convergent schemes for the calculation of bulk and surface Green functions, J. Phys. F: Met. Phys. **15**, 851 (1985).

[64] Q. Wu, S. Zhang, H.-F. Song, M. Troyer, and A. A. Soluyanov, WannierTools: An open-source software package for novel topological materials, Comput. Phys. Commun. **224**, 405 (2018).

[65] S. Xiong, B. Xi, C. Wang, G. Xi, X. Liu, and Y. Qian, Solution-phase synthesis and high photocatalytic activity of wurtzite ZnSe ultrathin nanobelts: A general route to 1D semiconductor nanostructured materials, Chem. Eur. J. **13**, 7926 (2007).

[66] M. Chen and L. Gao, Synthesis and characterization of wurtzite ZnSe one-dimensional nanocrystals through molecular precursor decomposition by solvothermal method, Mater. Chem. Phys. **91**, 437 (2005).

[67] P. Tronc, K. S. Zhuravlev, V. G. Mansurov, G. F. Karavaev, S. N. Grinyaev, I. Milosevic, and M. Damnjanovic, Optical properties of photodetectors based on wurtzite quantum dot arrays, Phys. Rev. B **77**, 165328 (2008).

[68] M. L. Cohen and J. R. Chelikowsky, Wurtzite structure semiconductors, in *Electronic Structure and Optical Properties of Semiconductors,* Springer Series in Solid-State Sciences Vol. 75 (Springer, Berlin, 1989), pp. 140–160.

[69] C.-Y. Yeh, Z. W. Lu, S. Froyen, and A. Zunger, Zinc-blende–wurtzite polytypism in semiconductors, Phys. Rev. B **46**, 10086 (1992).

[70] See Supplemental Material at http://link.aps.org/supplemental/10.1103/PhysRevB.103.094306 for additional details about phonon dispersions of different wurtzite *MX* chalcogenides in Figs. S1– S8, phonon surface arcs at the frequency of 6.48 THz in Fig. S9, phononic topological Weyl nodal lines in Figs. S10 and S11, and positions of Weyl phononic points in Table S1.

[71] P.-F. Liu, T. Bo, J. Xu, W. Yin, J. Zhang, F. Wang, O. Eriksson, and B.-T. Wang, First-principles calculations of the ultralow thermal conductivity in two-dimensional group-IV selenides, Phys. Rev. B **98**, 235426 (2018).

[72] P.-F. Liu, T. Bo, Z. Liu, O. Eriksson, F. Wang, J. Zhao, and B.-T. Wang, Hexagonal M_2C_3 (M = As, Sb, and Bi)

monolayers: new functional materials with desirable band gaps and ultrahigh carrier mobility, J. Mater. Chem. C **6**, 12689 (2018).

[73] H. Weng, X. Dai, and Z. Fang, Exploration and prediction of topological electronic materials based on first-principles calculations, MRS Bull. **39**, 849 (2014).

[74] A. Bansil, H. Lin, and T. Das, Colloquium: Topological band theory, Rev. Mod. Phys. **88**, 021004 (2016).

[75] S. L. Adler, Axial-vector vertex in spinor electrodynamics, Phys. Rev. **177**, 2426 (1969).

[76] A. A. Soluyanov and D. Vanderbilt, Computing topological invariants without inversion symmetry, Phys. Rev. B **83**, 235401 (2011).

[77] R. Yu, X. L. Qi, A. Bernevig, Z. Fang, and X. Dai, Equivalent expression of $\mathbb{Z}_2$ topological invariant for band insulators using the non-Abelian Berry connection, Phys. Rev. B **84**, 075119 (2011).

[78] H. Weng, X. Dai, and Z. Fang, Topological semimetals predicted from first-principles calculations, J. Phys.: Condens. Matter **28**, 303001 (2016).

[79] T. Qin, J. Zhou, and J. Shi, Berry curvature and the phonon Hall effect, Phys. Rev. B **86**, 104305 (2012).

[80] L. Zhang, J. Ren, J.-S. Wang, and B. Li, Topological Nature of the Phonon Hall Effect, Phys. Rev. Lett. **105**, 225901 (2010).